Carbohydrate Polymer Technologies and Applications 7 (2024) 100524

Contents lists available at ScienceDirect

Carbohydrate Polymer Technologies and Applications

journal homepage: www.sciencedirect.com/journal/carbohydrate-polymer-technologies-and-applications

Ready-to-print alginate inks: The effect of different divalent cations on physico-chemical properties of 3D printable alginate hydrogels

Giovanni Falcone [a], Stefan Schrüfer [b], Sonja Kuth [c], Pierluigi Mazzei [a], Salvatore De Pasquale [d], Pasquale Del Gaudio [a], Rita P. Aquino [a], Aldo R. Boccaccini [c,*], Paola Russo [a,*]

[a] Department of Pharmacy, University of Salerno, 84084 Fisciano, SA, Italy
[b] Department of Materials Science and Engineering, Institute of Polymer Materials, University of Erlangen-Nuremberg, 91058 Erlangen, Germany
[c] Institute of Biomaterials, University of Erlangen-Nuremberg, 91058 Erlangen, Germany
[d] Department of Physics E. R. Caianiello, University of Salerno 84084 Fisciano, SA, Italy

ARTICLE INFO

Keywords:
Alginate
Ionic crosslinking
Hydrogel-inks
3D printing

ABSTRACT

Studies about the use of different divalent cations to produce 3D printed scaffolds are almost limited to their application as secondary crosslinking agents after the printing of alginate. For this reason, this research aims to demonstrate the possibility to develop alginate hydrogel-inks for 3D-printing application, exploiting the ionotropic gelation in a preprint step, by paying attention to the role of divalent cations on hydrogel-inks properties. The investigation of transversal relaxation time highlighted differences among inks (barium-ink 90.04 ms, calcium-ink 84.33 ms, and zinc-ink 75.05 ms) suggesting a potential influence of different cations. If all the inks showed a shear thinning behaviour with similar flowability index (0.153±0.018), they were characterised by different consistency index (from 2420 to 574 Pa•s), extrudability and homogeneity, parameters that influence the printing setup. In fact, to reach the same flowability and thus low deviation in the layer width for all inks, a variation in printing pressure and speed was necessary. Overall, it can be deduced that alginate inks preparation following a preprint crosslinking approach could be a valid method to overcome the alginate printability issues underlining the possibility to select the crosslinking cation according to the technological properties wanted for the final matrix.

1. Introduction

Among the large range of natural polymers, alginate shows unique physico-chemical characteristics such as the pH-sensitive gel-forming ability or ability to develop a hydrogel in the presence of a crosslinking agent (Chan, Ching, Liew & Heng, 2007).

Thanks to this peculiarity, coupled with biocompatible and biodegradable properties, alginate is one of the most versatile natural polymers, used in a wide range of fields from food industry, to biomedical, as well as pharmaceutical areas (Farshidfar, Iravani & Varma, 2023; Jain & Bar-Shalom, 2014). In particular, alginate-based hydrogels are largely exploited in bioprocessing, drug delivery and chemical sensing as carrier matrix, able to modulate the release behaviour of biomolecules, active pharmaceutical ingredients (APIs) or cells (Amante et al., 2022; Boontheekul, Kong & Mooney, 2005; Srivastava & McShane, 2005).

Among the innovative applications of alginate hydrogels, there is certainly their potential use as ink for 3D printing process (Axpe & Oyen, 2016). However, the versatility of alginate for 3D printing is somewhat restricted and limited due to issues related with printability requirements such as low viscosity, weak mechanical performance, low matter content, and matrix homogeneity (Gao et al., 2018; Gutierrez et al., 2019; Sonego, Santagapita, Perullini & Jobbágy, 2016). Therefore, further studies are needed to find the best way to use alginate in 3D printing approaches, as confirmed by Mallakpour et al., who published a historical perspective review about the state-of-art of 3D printing technology of alginate-based materials (Mallakpour, Azadi & Hussain, 2021). To overcome these alginate printability issues, some approaches were investigated such as alginate chemical modification (Cai, Heid & Boccaccini, 2021; Wei et al., 2023), combination with other polymers (Giuseppe et al., 2018; Wang et al., 2021; Yang et al., 2018), or development of a preprint crosslinking procedure (Hazur et al., 2020; Tuladhar, Nelson & Habib, 2022). The feasibility of this latter approach was also demonstrated by our research group in a previous work (Falcone et al., 2022).

* Corresponding authors.
E-mail addresses: aldo.boccaccini@fau.de (A.R. Boccaccini), paorusso@unisa.it (P. Russo).

https://doi.org/10.1016/j.carpta.2024.100524

Available online 31 May 2024

On the other hand, in recent years, the application of metallic ions in medicine has become a hot research topic in regards to their application as drug release modifiers or antimicrobial agents (Hernández-Escobar et al., 2019; Ramya et al., 2015). If the mechanism of alginate gelation is still explained in terms of the original egg-box model, from mono-complexes to the egg-box dimers, and the laterally associated egg-box multimers (Braccini & Pérez, 2001; Cao, Lu, Mata, Nishinari & Fang, 2020; Mørch, Donati, Strand & Skjåk-Bræk, 2007; Fang et al., 2007), some novel insights to the influence of different crosslinking agents have been proposed in particular with a specific focus on the final properties of this hydrogels and their potential application (Donati & Christensen, 2023; Hu, Lu, Mata, Nishinari & Fang, 2021; Tan et al., 2023). Reig-Vano et al. recently published an article about the structural analysis of alginate beads based on calcium, copper and zinc as cross-linkers, highlighting that the beads formation behaviour was influenced by the cation used, calcium and zinc leading to a ionotropic gelation mechanism, while copper to a double mechanism i.e., ionotropic gelation and acid precipitation resulting in the production of beads with different shape and surface morphology (Reig-Vano et al., 2023). Cerciello et al. described the effect of cations (alone or in a blend) on the technological properties of alginate beads, showing that the substitution of calcium with zinc as crosslinking agent led to a matrix with lower swelling properties affecting the API release (Cerciello et al., 2017). Martsouka et al. showed the different biological activities of zinc and copper against bacteria and yeasts, highlighting the excellent results of Cu-modified bentonite against both species, while Zn-modified bentonite showed good results only against yeasts (Martsouka et al., 2021). Furthermore, cations have been used to develop three dimensional (3D) culture of living cells, as reported by Vigo et al. In their study, they exploited barium to produce alginate capsules for 3D immobilisation of living cells with peculiar technological properties such as mechanical properties and thus matrix permeability (Vigo et al., 2004).

This literature revision about alginate gelation highlighted a lack of knowledge on the use of different cations as crosslinking agents for alginate hydrogels development to be used as inks for 3D printing process obtained through preprint crosslinking step. In fact, at the moment, studies about the use of different divalent cations to produce 3D printed scaffolds are almost limited to their application as secondary crosslinking agent after the printing of alginate, or in form of nanoparticles loaded into the alginate matrix (Amaral et al., 2019; Hazur, Röder, Czwalinna, Schubert & Boccaccini, 2023; Tabriz, Hermida, Leslie & Shu, 2015).

Starting from this background, this study aims to investigate the feasibility to produce ready-to-print alginate inks paying attention to the effect of various divalent cations on the alginate hydrogels formation, speculating a relationship between physicochemical properties of obtained hydrogels and their final printing performance.

In this perspective, divalent cations can be exploited both as crosslinking agents to develop ready-to-print inks, as well as functional ingredients able to modulate the technological properties of final printouts, i.e., personalised drug dosage forms, supplementary dietary food, scaffolds for tissue engineering.

2. Materials and methods

2.1. Materials

Sodium Alginate (PH163S2, CAS) obtained from VIVAPHARM (JRS PHARMA GmbH & Co. KG, Rosenberg, Germany), was selected as the main component of the hydrogels. It was characterised by a M_w of 216 KDa and a M/G ratio of 1.06 (Karakaya et al., 2023). Calcium chloride dihydrate ($CaCl_2 \bullet H_2O$, "ACS reagent", M_w 147.01 g/mol, purity > 99 %, CAS 10035-04-8), Zinc chloride ($ZnCl_2$ "BioReagent", M_w 136.30 g/mol, purity > 95 %, CAS 7646-85-7), and Barium chloride dihydrate ($BaCl_2 \bullet H_2O$, "ACS reagent", M_w 244.26 g/mol, purity > 99 %, CAS 10326-27-9) were received from Sigma-Aldrich.

2.2. Methods

2.2.1. Hydrogel-inks preparation

Considering that the alginate-cations microstructure is a function of the molar ratio between calcium and glucuronic acid residues (R-value) as described by Fang et al., the exact cations concentration to obtain hydrogels characterised by egg-box multimeric structure ($R = 0.55$) was established (Fang et al., 2007). The alginate hydrogels were prepared following a procedure previously described (Falcone et al., 2022), with slight modifications: sodium alginate powder was hydrated in a pre-set volume of bi-distilled (bid) water to obtain a concentration of 4% w/v (Na/Alg), while each cation type was solubilised in the same amount of bid water to obtain a cation concentration of 45 mM. The crosslinking was carried out by mixing the alginate gel and the cations solution (1/1 v/v ratio) under homogenization (Ultra-Turrax® T25, IKAWorks GmbH & Co. Staufen, Germany) (10-000 rpm for 3′). The obtained hydrogels 2% w/v of alginate crosslinked with 22.5 mM of cation, i.e., calcium-alginate (H_Ca/Alg), barium-alginate (H_Ba/Alg), and zinc-alginate (H_Zn/Alg) were centrifuged (2500 rpm or 965xg for 10 min) to remove trapped air-bubble and then stored for 16 h at 4 °C to ensure the gel structuring by decantation (supplementary material, Fig. P1).

2.2.2. FT-IR

To detect chemical differences between the obtained matrices, infrared spectroscopic evaluation was performed using an attenuated total reflectance FTIR (ATR-FT-IR, IRAffinity-1S, Shimadzu Europa GmbH, Germany). The analyses of Na/Alg, H_Ca/Alg, H_Ba/Alg, and H_Zn/Alg were carried out in the spectral range of 4000–400 cm^{-1}, at a resolution of 1 cm^{-1} and 128 scans. To minimise the potential overlay of water signals in hydrate matrices, analyses were carried out using samples in form of powder: specifically, hydrogels were subjected to air drying until constant weight was reached (30 °C, around 6 h) obtaining polymeric films mortar milled before the analysis.

2.2.3. Magnetic resonance imaging (MRI) of crosslinked alginate hydrogels

All ^{1}H MRI experiments were performed on crosslinked hydrogels at 298 ± 1 K on a 300 MHz Bruker Avance wide-bore magnet (BrukerBiospin, Rheinstetten, Germany), equipped with a 1.5 mm μ-imaging MICRO 5 probe working at a ^{1}H frequency of 300.13 MHz. Each sample i.e., H_Ca/Alg, H_Ba/Alg and H_Zn/Alg was loaded into a 15 mm NMR tube and placed in a vertical position for 8 h to permit a homogeneous spatial distribution of the material before the analysis.

T_2 experiments were performed by applying an echo-train MSME (multi-slice-multi-echo) pulse sequence, setting 2.5 s of recycle delay, 12 scans, and acquiring 16 experiments with an increasing number of spin-echoes (total spin-echo time ranging within 14 and 168 ms). Data were fitted to a single exponential decay, according to the equation (Eq. (1)):

$$M_t = M_0 exp(-t / T_2) \quad (1)$$

where, M_0 and M_t represent the magnetization intensity resulting at the minimum spin-echo delay and after the i_{th} spin-echo interval, respectively. Spin density measurements were performed by considering the images obtained at the shortest echo-delay (14 ms).

T_1 measurements were acquired by RARE (Rapid Acquisition with Relaxation Enhancement) experiments, which consisted of 3 scans, a rare factor of 2, and increasing repetition times ranging within 0.286 to 22.5 s in 8 experiments. Data were fitted to a single exponential decay, according to the equation (Eq. (2)):

$$M_t = M_0[1 - \exp(-t / T_1)] \quad (2)$$

where, M_0 and M_t represent the magnetization intensity resulting at the full nuclear relaxation and after the i_{th} recovery delay, respectively.

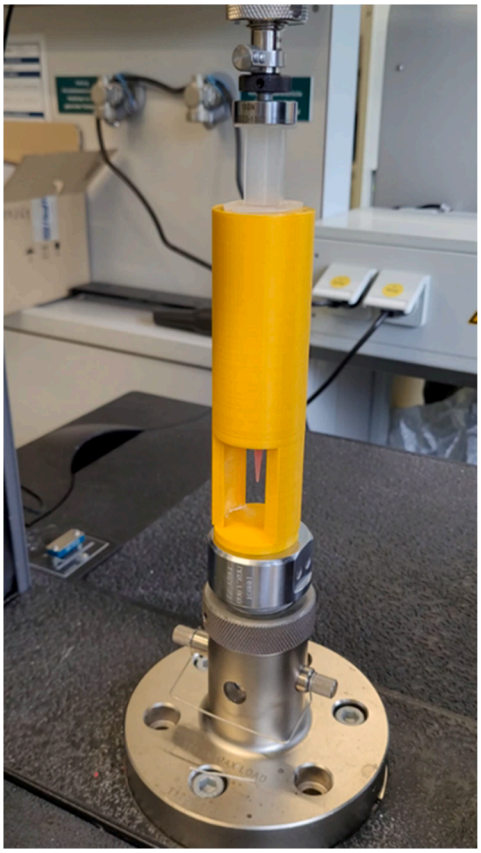

Fig. 1. Photo of Instron machine with complete set-up of 3D printed lab-made tool equipped with syringe and needle (lab-made tool dimensions: height 15 cm, width 4.5 cm).

The MRI images resulted from the acquisition of 8 interlaced axial slices with a width of 1.35 mm, a field of view of 1.33 × 1.20 mm^2, and 1.07 mm of slice-interdistance. The images consisted of a 256 × 256 matrix, for T_2 experiment, and a 128 × 128 matrix, for T_1 experiments. ParaVision 5.1 Bruker software was used to process MRI data, obtain all the images, and calculate T_1 and T_2 relaxation times. All calculations were conducted on nuclear data extrapolated from nine ROIs (Region Of Interests) per sample. Briefly, 3 representative slices per sample were considered (mostly the central ones) and, for each of them, 3 ROIs were selected, possibly accounting for possible spatial inhomogeneity and artefacts. The chosen ROIs consisted in two smaller (0.07 cm^2) and one larger (0. 74 cm^2) circular areas. T_1 and T_2 data were calculated for each single ROI and averaged for each sample (3 ROIs x 3 slices x sample) (supplementary material, Fig. P2).

The ANOVA (ANalysis Of VAriance) test was applied to assess the significance of differences (Tukey's Test at an α confidence level of 0.01) detected among the studied hydrogels and was carried out by the XLStat software (v.2019, Addinsoft, Paris, France). The letters A, B and C arbitrarily associated as symbols with T_1 and T_2 results, indicate whether the differences among the tested hydrogels are statistically significant (p-value < 0.01) or not. Specifically, results which differ significantly from each other were marked with different letters, while results which did not exhibit significant differences were marked with the same letter.

2.2.4. Rheological investigation

Discovery HR-2 Rheometer (TA Instruments Ltd., New Castle, Delaware, USA) equipped with a 20.0 mm 1.99028° cone plate was used to carry out the rheological characterization of hydrogels (T = 25 °C). The software used is Trios from TA Instruments. The rheological parameters i.e., viscoelastic shear moduli, elastic recovery, and shear stress were investigated via both oscillatory and transient test, to highlight the effect of cations variation on the inks physicochemical properties. Amplitude sweep test was performed in a shear strain "γ" range from 0.1 to 100 % (with constant angular frequency at 10 rad/s), to identify the Linear ViscoElastic Region (LVER) of each hydrogel (maximum of deformation set at 3 % drop of storage modulus value).

According to the results of the amplitude test, hydrogels were subjected to a frequency sweep test, varying the angular frequency "ω" from 100 to 0.1 rad/s. Complex viscosities were graphed as function of the angular frequency (logarithmic scale vs logarithmic scale). The resulting curves were fitted with a Power-Law function (Eq. (3)) (Adhikari, Perwez, Das & Saha, 2021)

$$\mu^* = K{\cdot}\omega\, exp\left(p^{-1}\right) \tag{3}$$

where μ^* is the complex viscosity, K is the consistency index (viscosity value at 1.0 rad/s), and p is the flow index ($p < 1$ means shear thinning behaviour).

Regarding the evaluation of transient properties, a creep and recovery test was performed. In detail, the deformation strain of each ink was evaluated when subjected to a constant stress of 3 Pa (stress value set in the LVER of amplitude sweep test, not damaging the samples structure) over a time-period of 60 s. After reaching a compressive strain, stress relaxation was recorded over the same timeframe set for the creep step.

All tests were performed in triplicate and the results were reported as mean value and standard deviations.

2.2.5. Inks extrudability: extrusion force and inks homogeneity

Mechanical tests were performed on an Instron instrument, equipped with a 3D printed lab-made tool (Fig. 1), developed to perfectly hold a 25 ml syringe. These tests results were elaborated exploiting two parameters i.e. Extrusion Force (EF) and Force Deviation (FD) (Cohen et al., 2010), that allowed to highlight the differences in inks extrudability.

The load cell selected for the test was 100 N, the displacement speed was set at 5 mm/min, the test duration was 40 s, and two different tips were evaluated i.e., 22 G (450 μm), and 20 G (580 μm). The analysis of each sample was performed in triplicate (n = 3), thus results of individual tests were then averaged together. The extrusion force (force required to obtain a continuous extrusion flow) was calculated as the mean of extrusion force over time. The force deviation was considered as the standard deviation of the extrusion force recorded with a timeframe of 20′ (after reaching steady state condition).

2.2.6. Printability investigation

The printing performance of developed inks, i.e., H_Ca/Alg, H_Ba/Alg, and H_Zn/Alg were investigated by analysing four specific outcomes: the Line Width Fidelity (LWF) in function of print speed, the time-dependant layer spreading, the Layer Stacking (LS), and the Printability index (P_i) (Fig. 2).

All printing tests were performed using as build plate a vaseline covered petri dish in order to minimise the surface charge interaction between hydrogels and build plate material (Falcone et al., 2023). To evaluate the line width fidelity, three different print speeds in a range from 15 to 25 mm/*sec* were tested for each hydrogel-ink. In detail, photos of printed lines were taken, using the BioX HD Camera Tool. Images were then analysed to measure the layer diameter. These values were compared to the nozzle diameter. The time-dependent layer spreading was evaluated following the method proposed by Sonnleitner et al. (Sonnleitner, Schrüfer, Berglund, Schubert & Lang, 2021). Photos of printed lines were taken at different times after printing i.e., after 5, 10, 15, 20, 25 s to measure the line width (mm) and quantify the layer spreading during this time. Moving to the evaluation of the multiple-layer printability, a two layer grid model was printed. To

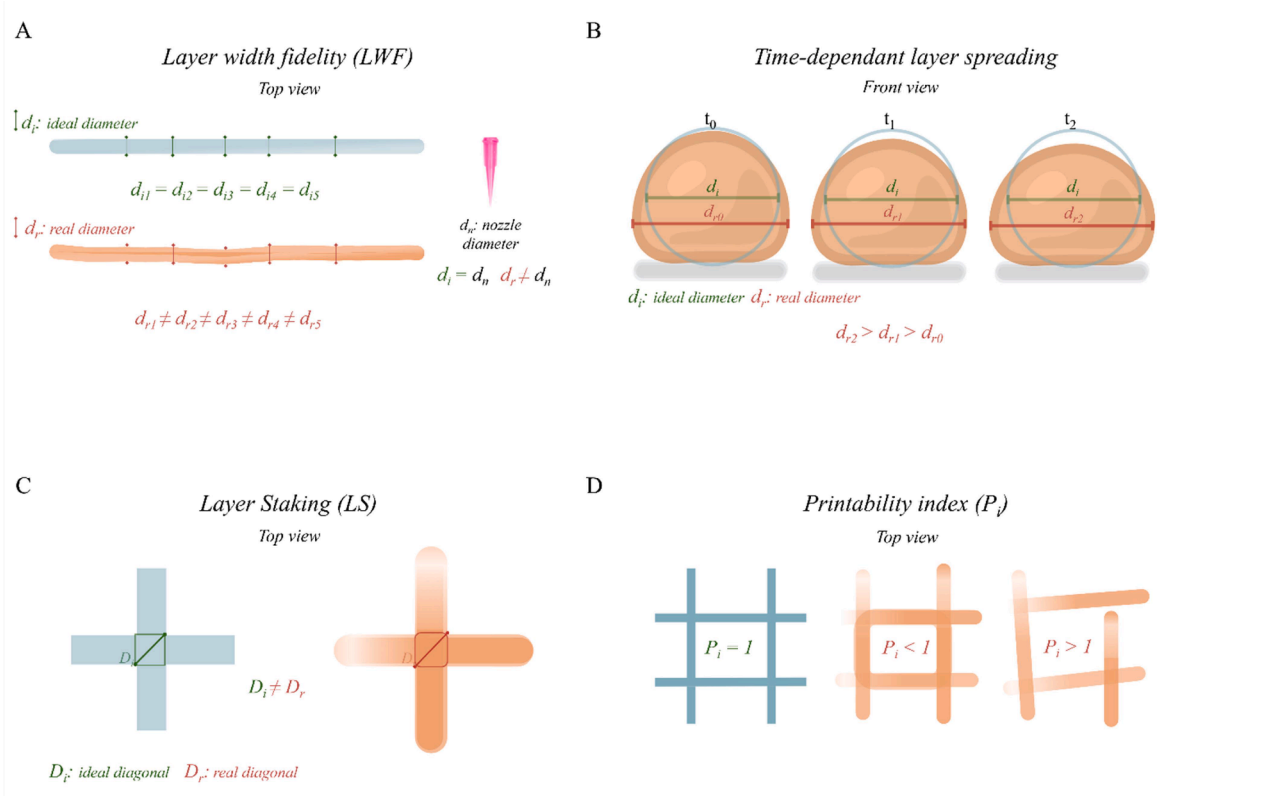

Fig. 2. Graphical description of the printing tests carried out to evaluate the hydrogel-inks printability: A) layer width fidelity; B) time-dependant layer spreading (both A and B were performed using single line model); C) layer stacking; D) printability index (both C and D were performed using a grid model).

evaluate the LS, images were acquired and analysed using an optical microscope (Carl Zeiss STEMI 508 microscope equipped with ZEN 3.2 software). The LS was measured as the fitting value between the diagonal square of each printed model and the diagonal square of the digital model (Bednarzig et al., 2022). The Pi value was calculated following the methods proposed by Unalan et al. (Eq. (4)) (Unalan, Schruefer, Schubert & Boccaccini, 2023):

$$\mathrm{Pi}(1) = \frac{\pi}{4C} \cdot 100 \tag{4}$$

where C is the circularity, an experimental value about the area of hollow printed square, calculated to be used later to analyse the Pi. The equation for C calculation is the following (Eq. (5)):

$$\mathrm{C}(1) = \frac{4\pi A}{p} \cdot 100 \tag{5}$$

where p is the perimeter of the hollow square of the grid printed model, and A is the area of the same square.

The software used for the images analysis was ImageJ, while linear regression and statistical investigation were conducted using GraphPad Prism 10 software. In detail, the ONE-WAY ANOVA test was conducted with the Tukey model for multiple comparison evaluations (α significance level 0.05, and confidence level of 95 %) *p-value*<0.05.

2.2.7. Platforms production: from digital development to printing process

The design of the final platform, a cylindric scaffold with base diameter of 20 mm and height of 12 mm, was developed *via* Rhinoceros 6 CAD software.

Slicing and printing optimization were carried out by the HeartOS 1.4 Software. The slicing process led to a slight modification of model height from 12 to 12.18 mm due to the balance between digital height and layer height. Most relevant slicing parameters are listed below:

Table 1
Main printing parameters optimised in accordance with the characteristics of each ink.

Inks	Printing parameter		
	Pressure (KPa)	Speed (mm/sec)	Temperature (°C)
H_Ca/Alg	28	18	25
H_Ba/Alg	31	18	25
H_Zn/Alg	36	22	25

Layer height: 580 μm
Initial layer height: 100 % of layer height (580 μm)
Infill density: 50 % of total surface area
Infill pattern: rectilinear

If the slicing parameters were the same for all the inks, the printing parameters were customised, in accordance with the results obtained by printability evaluation (Table 1).

The 3D-printing process of platforms was carried out using the BioX 3D-bioprinter by CellInk (CellInk, Sweden) using a petri dish covered with vaseline as build plate (Falcone et al., 2023).

2.2.8. 3D printed platforms resolution and reproducibility

The mass of printed platforms and the dimension fidelity were used as outcomes of printing resolution and reproducibility. The mass of printed platforms was weighed by analytical balance, while the diameter and the height were measured by digital calibre. The mean values of both platforms dimension were related to the dimension of digital model as percentage, i.e., printed platforms Diameter percentage "D_p" and printed platforms Height percentage "H_p":

$$\mathrm{D_p}(\%) = \frac{D\_(Printed\ model)}{D\_(Digital\ model)} \cdot 100 \tag{5()}$$

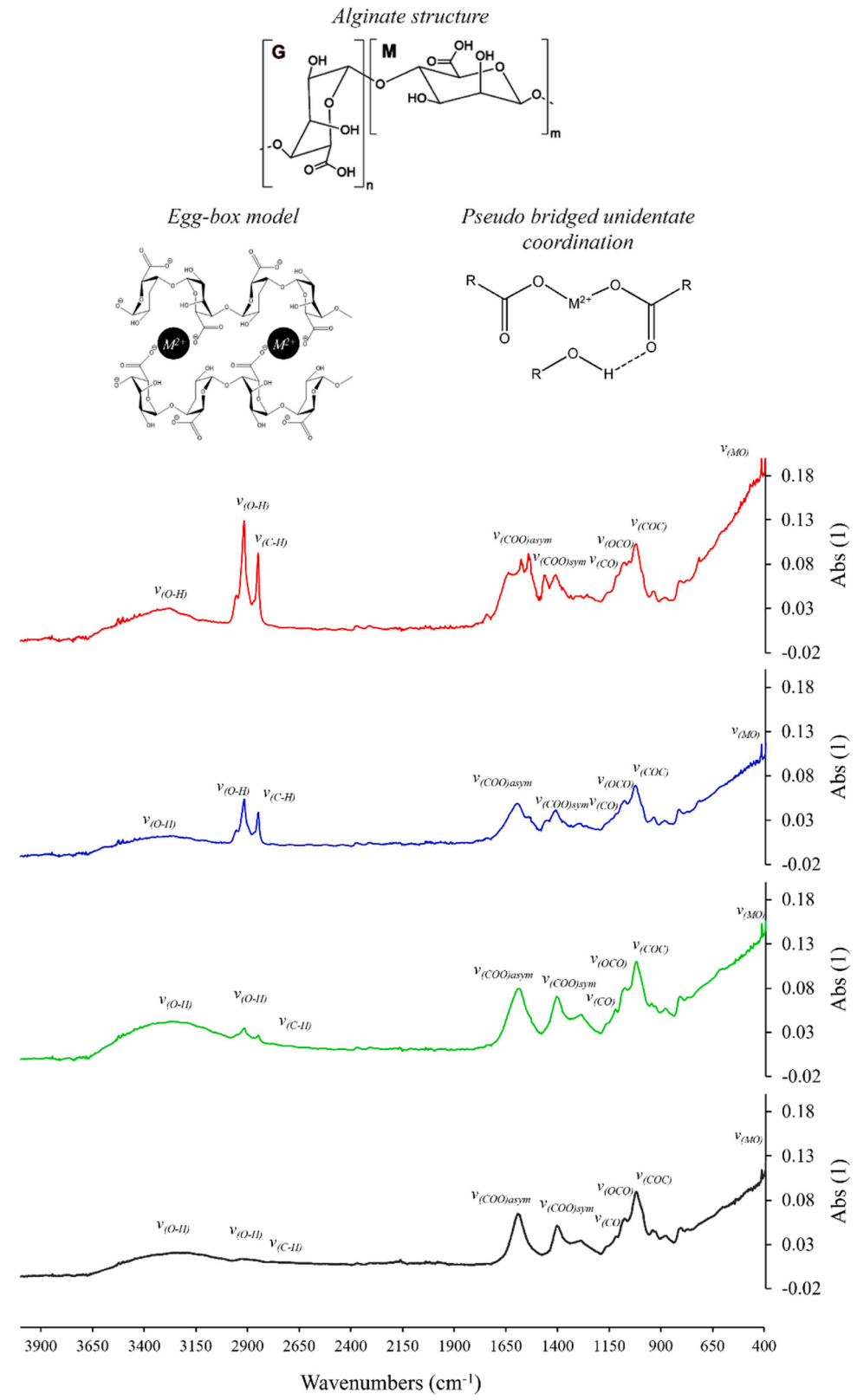

Fig. 3. Alginate chemical structure, both egg-box and pseudo bridged unidentate coordination models (Papageorgiou et al., 2010), and FT-IR spectrum of powdered dried films from: sodium-alginate gel (grey), zinc-alginate hydrogel (green), calcium-alginate hydrogel (blue), and barium-alginate hydrogel (red).

$$H_p(\%) = \frac{H\_(Printed\ model)}{H\_(Digital\ model)} \cdot 100 \quad (6)$$

At least 10 samples derived from each hydrogel-ink were evaluated.

3. Results and discussion

In a previous study conducted by our research group on the 3D printing application of alginate, a relationship between calcium

Table 2
Assignment of the main vibrational modes for sodium alginate and metal complexes, i.e., H_Ca/Alg,H_Ba/Alg, H_Zn/Alg.

	$\nu_{(O-H)}$	$\nu_{(C-H)}$	$\nu_{(COO)asym}$	$\nu_{(COO)sym}$	$\Delta\nu_{(COO)}$	$\nu_{(CO)}$	$\nu_{(OCO)}$	$\nu_{(COC)}$	$\nu_{(MO)}$
Na/Alg	2998–3667	2915	1603	1406	197	1125	1084	1024	417
H_Ca/Alg	3131–3665	2915	1587	1410	177	1117	1080	1026	419
H_Ba/Alg	3156–3657	2920	1582	1412	170	1121	1080	1028	419
H_Zn/Alg	3002–3657	2913	1582	1400	182	1125	1082	1026	419

concentration and alginate printability in function of alginate ionotropic gelation was observed (Falcone et al., 2022). In detail, it was highlighted that the monocomplex structure was not sufficient to satisfy the printing requirements, while reaching a laterally associated egg-box multimers entanglement, the alginate hydrogel becomes printable.

This entanglement can be reached by selecting a specific value of the ratio between crosslinking cation moles and the moles of glucuronic residues of alginate "R-value" ($R = 0.55$) (Fang et al., 2007). Moreover, the obtained alginate hydrogel was characterised by an interesting embedding capacity due to a three-dimensional network that could be exploited to use this hydrogel as carrier matrix for the delivery of drugs in 3D printed drug delivery systems. Considering the increasing interest about application of divalent cations such as zinc and copper in various field, i.e., pharmaceutical and biomedical field, this study aimed to evaluate the applicability of our preprint crosslinking procedure to obtain 3D printable alginate inks using different crosslinking cations (i.e., Ca^{2+}, Zn^{2+}, and Ba^{2+}) highlighting if the use of different cations led to changes in chemical entanglement and thus in the hydrogels properties, finding for each sample the optimised printing parameters.

Taking this R-value into account, three different hydrogels were prepared i.e., H_Ca/Alg, H_Ba/Alg and H_Zn/Alg.

3.1. Crosslinked alginate hydrogels characterization

FT-IR analysis was preliminary performed to show the effect of the -crosslinking process with all divalent cations (calcium, zinc, and barium) in comparison to sodium alginate (Fig. 3).

Sodium alginate spectrum exhibits characteristic bands due to: C—O stretching, (weak-sharp peak), stretching of C—O–C group, CHOH bending, COO– stretching with two sharp peaks related to both symmetric and asymmetric stretching, CH stretching in aliphatic structure, and OH stretching, usually described by a broad peak in a large range between 3000 and 3600 cm^{-1} influenced by hydrogen bounded of OH with water molecules) (Leal, Matsuhiro, Rossi & Caruso, 2008; Daemi & Barikani, 2012; Sartori, Finch, Ralph & Gilding, 1997). The most characteristic FTIR spectral bands and their assignments to the alginate and its metal complexes are reported in Table 2 (Al-Fakeh, Alazmi & El-Ghoul, 2023).

Literature about FT-IR investigation of metal-alginate complex reported different types of coordination, i.e., uncoordinate form, unidentate coordination, bidentate chelating coordination, and bidentate bridging coordination, described by the $\Delta\nu_{(COO)}$ complex (band difference of $\nu_{(COO)asym}$ and $\nu_{(COO)\ sym}$) in comparison to $\Delta\nu_{(COO)}$ sodium (Agulhon, Markova, Robitzer, Quignard & Mineva, 2012; Nakamoto, 1978). However, Papageorgiou et al. described a new model "pseudo bridged unidentate arrangement" that best fits with the egg-box theory also explaining the participation of hydroxyl group (adjacent to the carboxylic group) in the metal complexation (Papageorgiou et al., 2010). According to this hypothesis the $\Delta\nu_{(COO)}$ of each hydrogel was calculated (Table 2) highlighting an high similarity of values among sample in a comparable range with $\Delta\nu_{(COO)}$ sodium confirming the creation of complex with similar structure, in accordance with results proposed by Papageorgiou (Papageorgiou et al., 2010). The M-O bond stretching bands is evident in all the spectra around 419 cm^{-1} with similar intensity that is also influenced by the anionic counterion (chloride anion in all cases) (Dash, Gutti, Behera & Mishra, 2024). An interesting difference, that could allow us to detect differences among complexes due to the different cation used, was highlighted evaluating the changes in the OH stretching bands. In fact, in sodium alginate, as mentioned before, it is possible to observe only one broad band from 2998 to 3667 related to the presence of free water, as well as intermolecular and intramolecular hydrogen bonds that also affected the CH peaks identification. Differently, in all crosslinked samples it is possible to observe both the band in the range between 3100 and 3600 due to the presence of free hydroxyl groups, and a new peak around 2847 probably due to the implication of OH groups in the chelation complex (Socrates, 2004). Moreover, Fuks et al. suggested the role of hydrate ionic radius as a variable that influences the type of complexation, evidenced by the differences in the chelated OH peaks intensity detected in our samples (Fuks, Filipiuk & Majdan, 2006).

Starting from these results, MRI studies were performed to better understand the influence of each cation in the chemical interaction with alginate (Fig. 4).

Both colour tonality and pixel intensity in spin-density MRI images of H_Ca/Alg, H_Ba/Alg and H_Zn/Alg, appeared almost invariable, suggesting that, at a micro-meter level, the studied hydrogels did not significantly differ among each other. In fact, in all cases the corresponding integrations indicated a single and predominant proton population at a spin density of 197±3, with an intensity ranging within 1300 ±150 (supplementary material, Fig. P3). The high similarity of the results obtained confirmed the validity of the protocol followed for the production of crosslinked alginate hydrogels, taking into account the R-value. The egg-box-like multimeric-structure, in fact, was obtained for all the produced gels, regardless of the divalent cation used as crosslinking agent. However, a visual comparison revealed differences in terms of amount and size of air bubbles (pseudo-circular green areas). In particular, H_Ca/Alg, compared to H_Ba/Alg and H_Zn/Alg, exhibited a relatively lower number of bubbles, also characterised by a smaller size. Assuming that the procedures to produce the investigated gels and load them into the NMR tubes were the same, this different bubbles distribution may be correlated with hydrogels mechanical and viscoelastic properties, influenced by cation type.

Moreover, the evaluation of proton nuclear relaxation times permits to investigate, at a nanoscale level, the complex dynamics influencing the way and the rate with which the water excited nuclei transfer and lose the energy to recover the equilibrium α-state during MRI experiments. Being the nuclear relaxation rates dependent on the specific environment experienced by the excited nuclei, they can ultimately inform on properties related to structural scaffolds with which examined water molecules interact.

Relaxation spin-lattice (T_1) and spin-spin (T_2) times of H_Ca/Alg, H_Zn/Alg and H_Ba/Alg are shown in Fig. 5.

T_1 values exhibited an average value of 3465 ± 150 ms. Although H_Ca/Alg showed a significantly lower value compared to the other hydrogels, the differences were not enough to speculate any relevant inference on structure properties. Generally speaking, being T_1 constant mostly influenced by intermolecular polarisation exchanges and spin-lattice release of energy, this outcome confirms the macroscopic similarities among materials already observed through spin-density images (Fig. 5). Conversely, T_2 values varied significantly, as a function of hydrogel type, with values of 90.04, 84.33 and 75.05 ms for H_Ba/Alg, H_Ca/Alg and H_Zn/Alg, respectively. The longest transversal relaxation time recorded for H_Ba/Alg was attributed to a stronger rigidity of the material, accompanied by a structural scaffold enabling the confinement

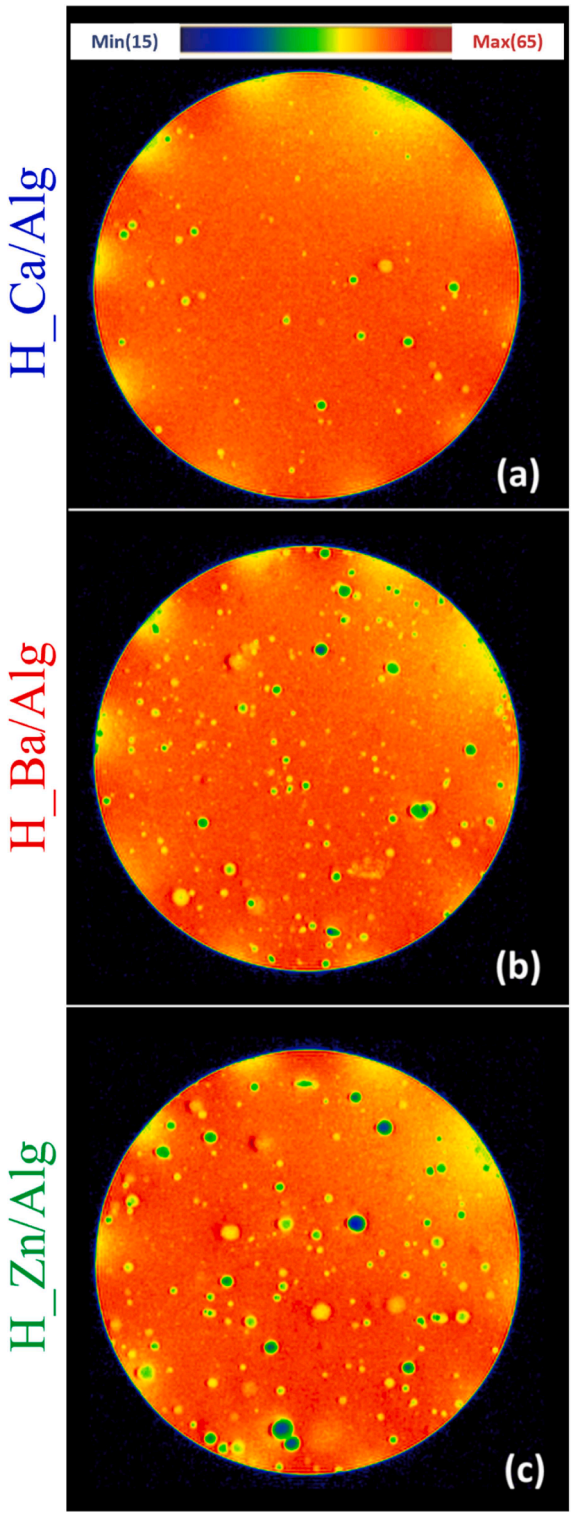

Fig. 4. MRI images of a representative central axial slice of alginate hydrogels obtained by using calcium (a), barium (b) and zinc (c) as crosslinkers, i.e. H_Ca/Alg, H_Ba/Alg and H_Zn/Alg. The images were acquired through an MSME pulse sequence and resulted from a total spin-echo time of 14 ms. The colour scale indicates the relative spin intensities, ranging from lower (MIN, dark blue, intensity value 15) to higher (MAX, red, intensity value 65) values.

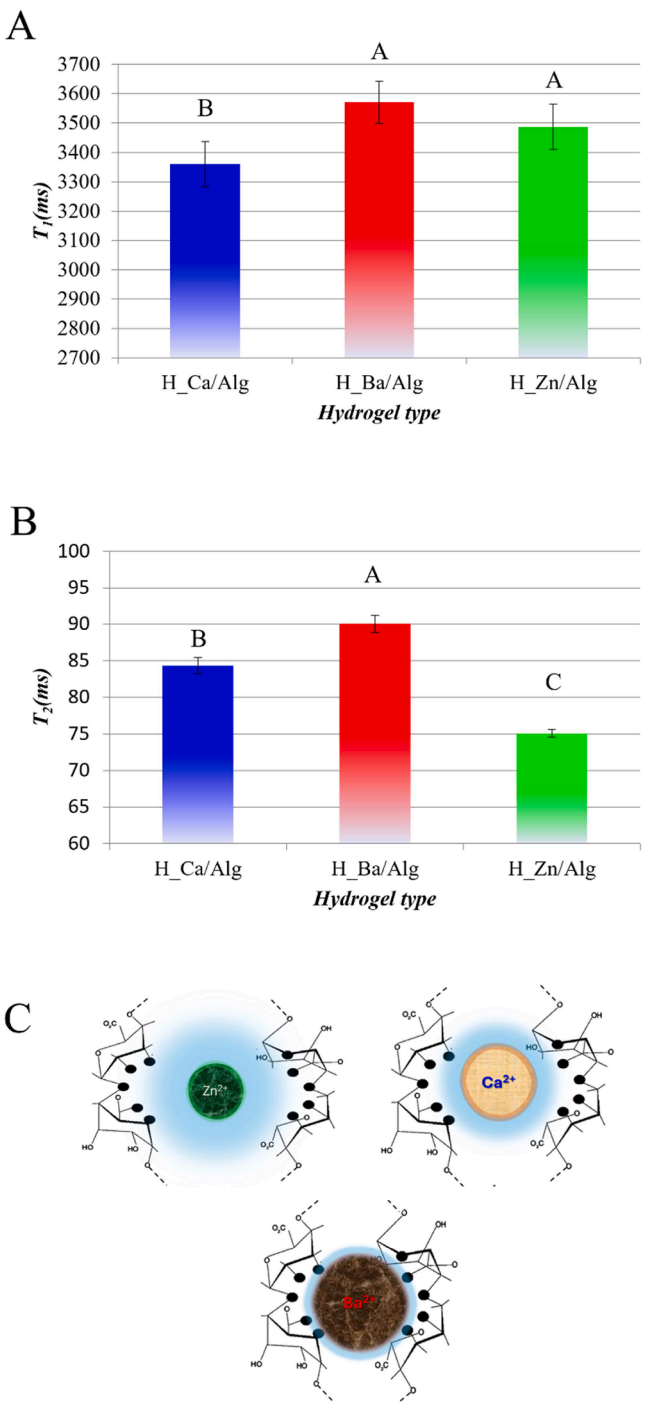

Fig. 5. (A) Longitudinal spin-lattice T_1 (ms) and (B) transversal spin-spin T_2 (ms) relaxation times of alginate hydrogels H_Ca/Alg, H_Ba/Alg and H_Zn/Alg. The histograms indicate the average value (n= 9) and the respective standard deviation. Figures include the standard deviation, as well as the results of ANOVA Tukey's test (red letters A-C), where hydrogels with no common letters are significantly different from each other at a 0.01 confidence level (99 % of significance). (C) Representative depiction of the spatial extent of Zinc, Calcium, and Barium hydrodynamic volumes (light blue area surrounding each nucleus) affecting the interacting forces involved in the alginate crosslinking.

of a relatively larger amount of free-like water (characterised by longer T_2 values). On the other hand, spin-spin relaxation values for H_Ca/Alg and H_Zn/Alg were found to be significantly shorter compared to H_Ba/Alg. This may be due to the ionic radii of these cations which are progressively bigger (zinc<calcium< barium). Although all of these nuclei showed two positive charges, they undergo a different distribution, as a function of ionic radius, with the smallest zinc attracting the largest number of water molecules. The water molecules hydrating the cations exhibit a limited mobility, which favours a more enhanced spin-

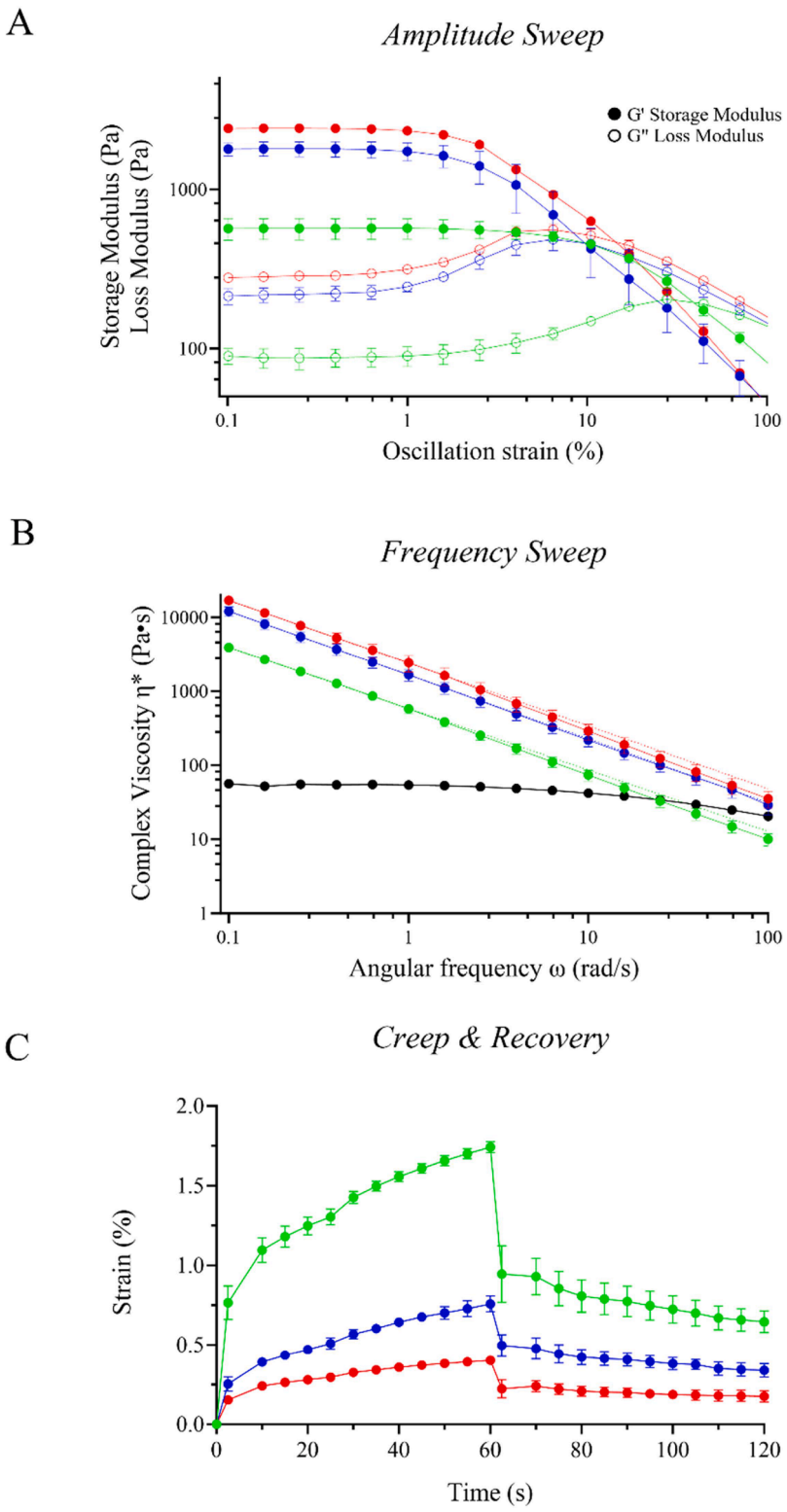

Fig. 6. Results of rheological investigation. A) amplitude sweep test, B) frequency sweep test, and C) creep & recovery test. Na/Alg (black), H_Zn/Alg (green), H_Ca/Alg (blue), and H_Ba/Alg (red).

spin relaxation process. This explains the T_2 shortening observed for H_Zn/Alg. Moreover, the relatively larger number of hydration water molecules increases the distance between structural Zn nuclei and carboxylic groups of G-Units, thus decreasing the mutual Coulombic attraction. This may reflect in the weakening of the H_Zn/Alg structure (or, at least, the determination of a less rigid structure).

After a structural characterization of crosslinked alginate matrices that allow to identify chemical differences among them, an accurate rheological investigation was carried out to understand how the structural differences affected the flow properties of each hydrogel-ink and thus their applicability in 3D printing (Fig. 6). Several studies underline the strictly relationship between rheological characteristics of hydrogels

Table 3
Rheological parameters of crosslinked alginate hydrogels by amplitude sweep test.

	G' at rest (Pa)	tan(δ) at rest (1)	Limit of LVER (%)	Flow point (Pa)
H_Ca/Alg	1792 ± 196	0.123	1.59	460
H_Ba/Alg	2414 ± 159	0.116	1.21	465
H_Zn/Alg	568 ± 85	0.146	2.52	195

and their 3D printability (Matas, Molina-Montero, Igual, García-Segovia & Martínez-Monzó, 2022; Herrada-Manchón, Fernández & Aguilar, 2023). For example the shear-thinning behaviour of inks is defined as a crucial requirement for their extrudability from the reservoir through the nozzle with changes of diameter section. Moreover, the viscoelasticity, investigated by oscillatory analyses, is essential for the shape retention ability of extruded filament when the pressure is stopped (Gillispie et al., 2023; Jackson & Dickens, 2021;; Schrüfer, Sonnleitner, Lang & Schubert, 2020).

In Fig. 6A results of amplitude sweep tests are reported, with both storage (G') and loss (G'') moduli (means and standard deviations) of the different hydrogels over shear strain. All crosslinked hydrogels were characterised by viscoelastic behaviour, a crucial requirement for hydrogels semi solid extrusion 3D printing application (Paxton et al., 2017; Townsend, Beck, Gehrke, Berkland & Detamore, 2019). In addition to the general evaluation of gel-like character, several rheological parameters have been taken into account as predictive indicators of an ink's printability, i.e. loss factor, complex modulus, yield point, and others (Schwab et al., 2020; Matas, Molina-Montero, Igual, García-Segovia & Martínez-Monzó, 2022). Among these, tan(δ) was one of the parameters widely used to potentially describe the relationship with ink printability, as suggested by Gao et al. who defined a " tan(δ) printing range" between 0.25 and 0.45 (Gao et al., 2018). However, one single parameter like tan(δ) is not sufficient to predict the printing behaviour of inks, since it depends on a multiplicity of factors, such us working temperature, or inks form, (i.e. thermoplastic inks, paste inks, colloidal dispersion inks, or, as in our case, crosslinked hydrogels). For example, Hu et al. demonstrated the good printability of ink with tan(δ) around 0.05, underlining the absence of a rheological parameter able to universally predict the printability (Hu et al., 2021). In the case of all alginate crosslinked inks, the tan(δ) mean value was 0.128 with low difference (± 0.018) highlighting that the cationic crosslinking procedure led to obtaining hydrogels with a similar consistency. Starting from these consideration, to compare the rheological characteristics of hydrogels due to different crosslinking cations used aiming to relate them with final printing performance, four parameters were considered, i.e. the storage modulus at rest, the loss angle tan(δ) at rest, the limit of LVER, and the flow point (Table 3).

Taking these parameters into account, it is possible to notice that the use of barium led to the hydrogel with the highest viscosity, characterised by the highest G' value, the lowest loss factor, highest flow point, and lowest LVER. These results are in agreement with the MRI results about the influence of barium on hydrogel structural strength. If H_Ca/Alg showed properties similar to H_Ba/Alg (similar LVER, and loss factor), a remarkable difference in the increase of the G''-curve slope (between the limit of LVER and flow point) was detected (Fig. 6A). The rising of the G''-curve indicates the occurrence of more relevant microcracks in the hydrogel matrix. Micro-cracks are phenomena of internal friction in specific areas of matrix related to the slow-motion process, higher G'' value means a larger number of micro-cracks in large areas of the matrix (Mezger, 2020). Nevertheless, the relevant decrease in the G' of H_Zn/Alg in comparison to the others, the value is in the range between 100 and 10,000 Pa, generally considered as the acceptability range for printing application (Zhang, Pandya, McClements, Lu & Kinchla, 2022).

Table 4
Results of Power-Law regression studies of crosslinked alginate hydrogels.

	K (Pa•s)	*P* (1)	R^2 (1)
H_Ca/Alg	1655	0.136	0.9764
H_Ba/Alg	2420	0.151	0.9890
H_Zn/Alg	574	0.171	0.9898

The performed oscillatory frequency sweep test allowed to obtain information on the materials behaviour and thus their 3D printability. In fact, non-Newtonian fluids, like polymer solutions, hydrogels, or colloidal suspension are classified into pseudoplastic fluids, characterised by shear thinning behaviour, or dilatant fluids, characterised by shear-thickening. In extrusion printing, shear-thinning is related to the ease of inks extrusion and maintaining of printed shape (Kiyotake, Douglas, Thomas, Nimmo & Detamore, 2019). As it is possible to observe in Fig. 6B, all samples showed a more pronounced shear thinning behaviour in comparison with non-crosslinked alginate gel, described by the decrease in complex viscosity of several orders of magnitude. This difference between alginate gel and crosslinked hydrogels underlines again the positive impact of the preprint crosslinking process on the development of 3D printable alginate matrices. From a structural point of view, the acquisition of shear thinning behaviour in crosslinked hydrogels is due to the chain disentanglement and macromolecular orientation along the shear flow when subjected to external pressure (Stojkov, Niyazov, Picchioni & Bose, 2021). To obtain more detailed info about the flow properties of each produced hydrogel, Power-Law model was used to perform a fitting study on the results of the frequency sweep test (Adhikari et al., 2021). This model is one of the most used approaches due to its ability to approximately describe the behaviour of a real non-Newtonian fluid using two parameters: the material consistency (K) and the flow behaviour index (p, $p < 1$ shear thinning behaviour, while $p > 1$ shear thickening behaviour) (Table 4).

The most relevant information about viscoelastic properties of hydrogels that could allow to predict the hydrogel printability was obtained by creep-recovery experiments, as they allow to show physicochemical responses of the hydrogel network to applied forces (Fig. 6C). In fact, the recovery-ability of hydrogel matrices is a crucial requirement for their applicability in 3D printing, because it influences the fiber self-standing after extrusion and thus the final resolution of the printing process. In the first step, this test describes the tolerance of a material that deforms when a constant static load is applied, which is also known as compliance. Then, the stress is removed to record the recoverability of hydrogels over a certain fixed time. All the crosslinked hydrogels showed a maximum deformation (γ_{max}) lower than their respective limit of LVER (Table 3). H_Ba/Alg and H_Ca/Alg were characterised by similar ideal elastic components (deformation occurring immediately after the beginning of the test) around 35 % of γ_{max} and an elastic recovery around 55 % of γ_{max}. The most relevant differences between H_Ba/Alg and H_Ca/Alg are related to the different time required to reach the constant rate of deformation (i.e., when the γ-curve is showing a constant slope angle). It is shorter for H_Ba/Alg, explaining the more relevant impact of purely viscous deformation in comparison to the viscoelastic deformation. Differently, H_Zn/Alg showed a purely elastic deformation value of around 45 % and a higher recovery portion around 65 %. These differences could be related to the weakness of the H_Zn/Alg structure, as described by NMR studies, but also to the high matrix homogeneity. In conclusion, all crosslinked hydrogels were characterised by a relevant elastic portion that ensures a fast recovery higher than 50 %, giving adequate structural rigidity to the matrix after deposition.

Although rheological evaluation is useful to obtain information about hydrogels viscoelastic properties and flow behaviour, it is not sufficient to predict the real hydrogels printing performance (Gómez-Blanco et al., 2023; Smith, Basu, Saha & Nelson, 2018). For this

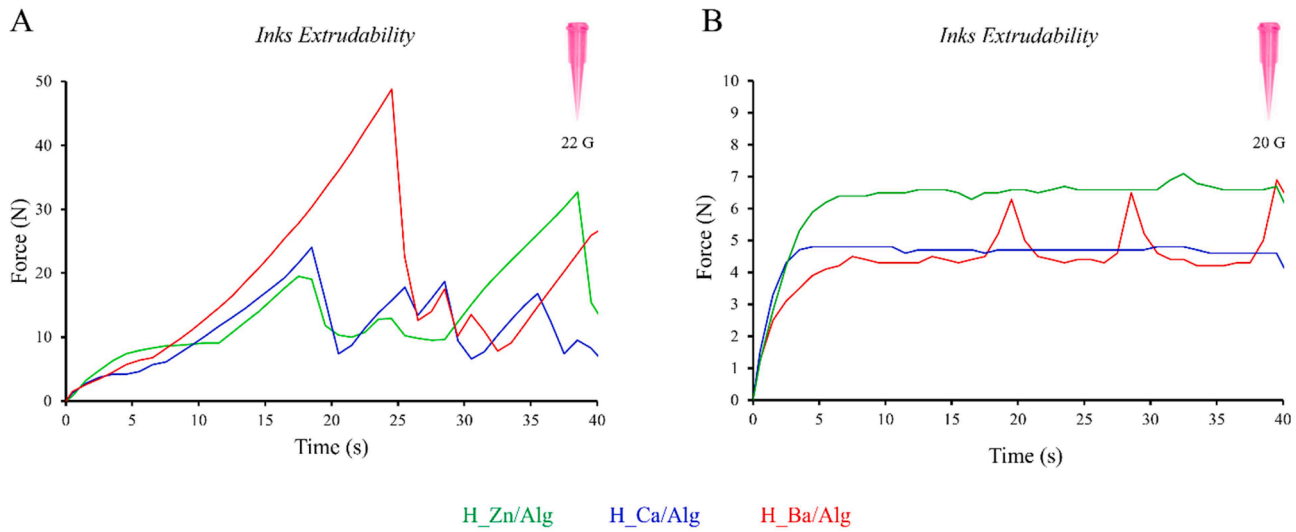

Fig. 7. Graphs about extrusion force over time of H_Zn/Alg (green), H_Ca/Alg (blue), and H_Ba/Alg (red), A) 22 G conical needle, B) 20 G conical needle (only one representative test for each sample is reported).

Table 5
Mean values of extrusion force and related force deviation.

Inks	Needle diameter	
	20 G	
	Extrusion Force (N)	Force deviation (N)
H_Ca/Alg	4.60	0.43
H_Ba/Alg	4.85	1.12
H_Zn/Alg	6.30	0.41

reason, we developed a mechanical test able to give information about inks extrudability. To perform this test, it was necessary to develop a tool holding a syringe or cartridge equipped with a needle, mimicking the extrusion during the Semi Solid Extrusion 3D printing process (SSE-3DP). The assumption behind the methodology of this test is the following: the force required to achieve a constant extrusion flow (namely extrusion force) depends on displacement rate, flow cross-section (dimension of needle orifice), material properties, and sliding friction due to the cartridge characteristics. If both, displacement rate and flow cross-section are held constant, the sliding friction is considered negligible and material characteristics become the only parameter influencing the extrusion force over the time. According to the theoretical assumption previously described, the mechanical test was performed with two different needle sizes i.e., 22 G, and 20 G. The test results were graphed extrusion force (N) over time (Fig. 7).

Fig. 7A shows the extrusion force recorded using the smallest needle (22 G). For all samples it is not possible to identify a plateau region of extrusion force, suggesting that microstructures of crosslinked alginate hydrogels are large in comparison to the needle diameter, negatively affecting the inks extrudability. Differently, the curve obtained from extruding inks through 20 G needle (Fig. 7B) showed a continuous extrusion flow reaching a force steady state condition. In the timeframe of steady state (force plateau), the fluctuation in extrusion value can be exploited to evaluate the matrix homogeneity, quantified by the standard deviation of extrusion force named as force deviation (Table 5).

H_Zn/Alg showed the highest extrusion force in comparison to the others, with an increase of around 30 %. This increase in the extrusion force could be related to the higher matrix homogeneity highlighted for zinc hydrogel. However, H_Ca/Alg and H_Zn/Alg showed a force deviation lower than 0.5 N underlining good matrix homogeneity (around 10 % of extrusion force) that could be considered acceptable to ensure the success of the printing process (Cohen et al., 2010). While focusing

Table 6
Established printing pressure value and extruded mass. If no need for pressure optimisation was detected, the dash was used as marker.

Inks	Calculated pressure (KPa)	Throughput (mg/sec)	Optimised printing pressure	Optimised throughput (mg/sec)
H_Ca/Alg	28	7.15 ± 0.69	–	–
H_Ba/Alg	28	6.23 ± 1.54	31	7.08 ± 0.63
H_Zn/Alg	36	7.30 ± 0.59	–	–

the attention on the results on H_Ba/Alg extrudability (Fig. 7B, needle 20 G), it is possible to notice the presence of peaks that describe increases of extrusion force during the extrusion procedure (with a force deviation higher than 1 N), likely due to hydrogel matrix reconstruction that negatively affects the continuous extrusion flow (Müller et al., 2020). This variation might be explained assuming the possibility that during the extrusion, the egg-box structures could interact among them, forming aggregates with final sizes next to the needle orifice, that can cause clocking phenomena and consequently flow instability.

3.2. Hydrogel-inks printability evaluation and optimization

Starting from the results of the mechanical tests, we attempted to relate the extrusion force with printing pressure exploiting the following equation (Eq. (7)):

$$Printing\ pressure\ (KPa) = \frac{Extrusion\ Force\ (N)}{Surface\ (mm^2)} \quad (7)$$

where the surface is the contact surface of the piston with the gel in 3 ml Cell Ink cartridges (175 mm^2). The calculated printing pressures are reported in Table 6. As proof of confidence of the method developed, the throughput of each ink was evaluated, weighing the material extruded during a 5-second period. The test was repeated 5 times for each ink, and the result was reported as the mean value of extruded mass *per* second.

The high fluctuation in extrusion force and force deviation observed for H_Ba/Alg in mechanical tests is also confirmed by H_Ba/Alg resulting throughput, 1 mg/*sec* lower than H_Ca/Alg and H_Zn/Alg throughput. With the aim to reach the same throughput with all hydrogel-inks, the printing pressure of H_Ba/Alg was increased from 28 to 31 KPa,

A

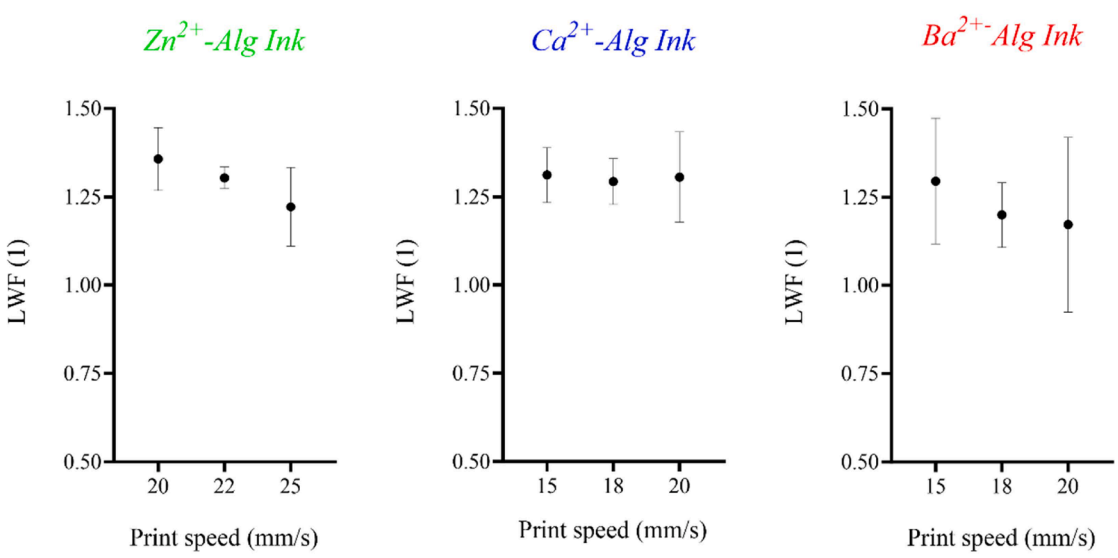

B

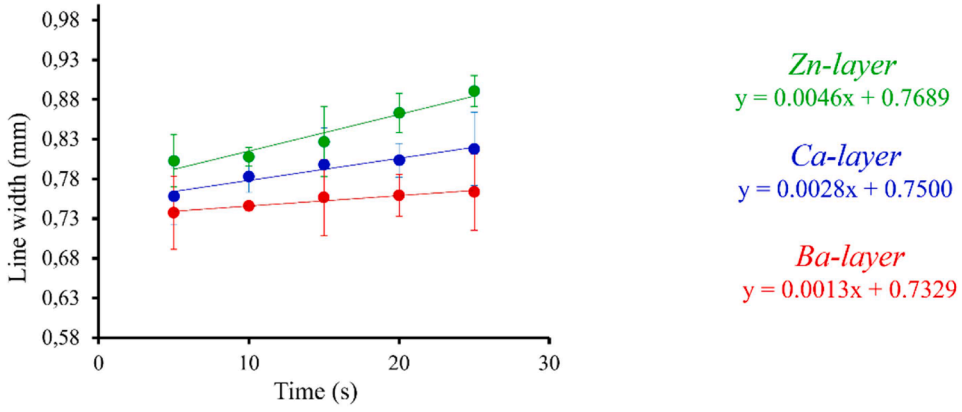

C

Inks	*Visual*	*Layer Staking (1)*	*Circularity (1)*	*Printability index (1)*
Standard		1	1	1
H_Zn/Alg	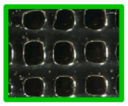	1.88	0.90	0.87
H_Ca/Alg	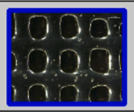	2.15	0.88	0.89
H_Ba/Alg	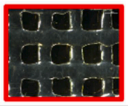	2.23	0.85	0.91

Fig. 8. Results about printability investigation of H_Zn/Alg (green), H_Ca/Alg (blue), and H_Ba/Alg (red). A) Layer width fidelity as function of print speed, B) time-dependant layer spreading, and C) resuming table of layer stacking and printability index.

Table 7
Digital photo, mass evaluation and morphological analysis of printed platforms.

	Visual	Mass (mg)	D_p (%)	H_p (%)
P_Ca/Alg	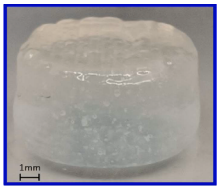	1879.3 ± 153.4	103.2 ± 0.7	94.2 ± 4.0
P_Ba/Alg	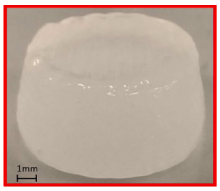	1898.0 ± 249.2	105.1 ± 1.9	95.3 ± 8.3
P_Zn/Alg	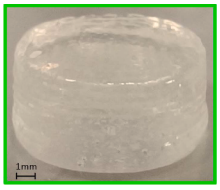	1916.5 ± 56.3	102.5 ± 0.7	95.9 ± 2.8

*.

obtaining optimised throughput with around 7 mg/sec (7.08 ± 0.63 mg/sec).

After the establishment of the optimal printing pressure of each alginate hydrogel-ink, the investigation was shifted to the printing performance evaluation in function of print speed, since an optimal balance between printing pressure and print speed allows for high printing resolution (Schubert, 2022). The LWF was considered as an outcome to quantify the impact of print speed. Three different print speeds were examined for each hydrogel-ink (Fig. 8).

From a macroscopic point of view, all inks showed a similar LWF value in a range between 1.17 and 1.35, with an increase of about 30 % of the layer diameter in comparison to the nozzle diameter (Fig. 8A). This increase is expected in consideration of the poor matter content of polymeric hydrogels that led to partial structural collapse (Leppiniemi et al., 2017). Focusing on the impact of different print speed, no statistically significant differences in LWF were detected, suggesting that the 5 mm/*sec* variation did not significantly affect the layer deposition and thus the printing resolution (Fig. 8A). Consequently, the selection of print speed was based on the evaluation of LWF standard deviation selecting the print speed for each ink related to the lowest standard deviation value. To better understand the differences in layer self-standing ability of crosslinked alginate hydrogels due to the different crosslinking cation, the layer spreading over time was also investigated (Sonnleitner et al., 2021). The slope value of resulting linear equations allowed us to estimate the different behaviour (Fig. 8B). H_Ba/Alg showed the lowest slope, meaning the best layer self-standing in time, followed by calcium hydrogel-ink, and finally the H_Zn/Alg, which showed the highest slope increase and thus the largest layer accommodation. These results confirmed the results about the different bound strength and viscoelastic properties observed during both MRI and rheological studies. The other parameter used to evaluate the layer self-standing ability during the printing process was the layer stacking, which allows to describe the layer deformation at the intersection of two layers due to the impact of both gravity force and surface tension (Fig. 8C) (Wang, Xu, Luo, Zhou & Si, 2018). As expected from previous results, all inks showed a layer stacking value higher than 1. However, the trend among inks is the opposite of LWF. H_Ba/Alg showed an increase of diagonal square 1.2 times higher than H_Zn/Alg, similar to H_Ca/ALg (1.15). Taking the results of MRI into account, this variation could be explained by the differences in cation charge and hydrogels surface charge (Li, Tan, Liu & Li, 2018). As a summary of hydrogels printing performance, the printability index was calculated (Fig. 8C). The obtained values were in the range between 0.9 and 1.1 that underlines the good printability. (Ouyang, Yao, Zhao & Sun, 2016; Unalan et al., 2023). Obtained results demonstrated one more time the potentiality of our preprint crosslinking approach to develop 3D printable alginate hydrogel-inks with different crosslinking cations. In fact, the P_i value was similar for all tested inks. Taking all the info obtained by printability investigations into account, a specific printing set-up for each hydrogel-ink was optimised to print cylindric platforms and evaluate both resolution (diameter and height in comparison to the digital model) and reproducibility of the printing process (Table 7).

At this time, no regulatory guidelines in the pharmaceutical field are available about the manufacturing quality of the printing process. For this reason, the printing reproducibility was carried out following the mass uniformity test described in European Pharmacopoeia 9th Edition. If the mean mass of all printed platforms was similar (with a minimum variation around 20 mg), relevant differences were detected in the reproducibility of the process with different hydrogel-inks. P_Ba/Alg were characterised by excessive mass variation (higher than 20 %) and therefore outside the pharmacopoeia limits. This expectable fluctuation of printed mass, almost due to the poor matrix homogeneity, could be overcome using hydrophilic plasticiser agent able to modulate the entanglement strength and thus the macroscopic flow properties of matrices (Hafezi, Scoutaris, Douroumis & Boateng, 2019; Falcone et al., 2023). Differently, P_Ca/Alg and P_Zn/Alg comply with the Pharmacopoeia requirements about the mass reproducibility. Concerning the dimensional resolution, all platforms showed deviations lower than 10 % in comparison to the digital model and thus the printing process can be defined as accurate.

4. Conclusion

Advanced analytical techniques allowed to highlight the differences in the physico-chemical properties of alginate matrix due to the use of different cations (i.e., Ca^{2+}, Ba^{2+}, and Zn^{2+}) and demonstrated how these differences affect both rheological and mechanical behaviour of the obtained hydrogels. Nevertheless, the knowledge of their specific properties allowed us to perform an optimal printing setup for each hydrogel-ink (i.e., printing pressure and speed), as confirmed by the printing accuracy observed during the production of the platforms.

This deep knowledge of gel printability and derived matrix compositions represents an important tool for the ever more researchers involved in the 3D printing of natural polymers such as alginate, not only for drug delivery platform production but also for bioprinting applications. Finally, the use of different cations represents an added value, giving the possibility to select the crosslinking agent according to the final application desired for the 3D printouts.

CRediT authorship contribution statement

Giovanni Falcone: Writing – original draft, Investigation, Formal analysis, Data curation. **Stefan Schrüfer:** Formal analysis, Data curation. **Sonja Kuth:** Formal analysis, Data curation. **Pierluigi Mazzei:** Formal analysis, Data curation. **Salvatore De Pasquale:** Writing – review & editing, Investigation. **Pasquale Del Gaudio:** Writing – original draft, Data curation. **Rita P. Aquino:** Writing – original draft, Data curation. **Aldo R. Boccaccini:** Writing – original draft, Supervision, Conceptualization. **Paola Russo:** Writing – original draft, Supervision, Funding acquisition, Data curation, Conceptualization.

Declaration of competing interest

The authors declare that they have no known competing financial

interests or personal relationships that could have appeared to influence the work reported in this paper.

Data availability

Data will be made available on request.

Supplementary materials

Supplementary material associated with this article can be found, in the online version, at doi:10.1016/j.carpta.2024.100524.

References

Adhikari, J., Perwez, M. S., Das, A., & Saha, P. (2021). Development of hydroxyapatite reinforced alginate–chitosan based printable biomaterial-ink. *Nano-Structures & Nano-Objects, 25*, Article 100630.

Agulhon, P., Markova, V., Robitzer, M., Quignard, F., & Mineva, T. (2012). Structure of alginate gels: Interaction of diuronate units with divalent cations from density functional calculations. *Biomacromolecules, 13*(6), 1899–1907.

Al-Fakeh, M. S., Alazmi, M. S., & El-Ghoul, Y. (2023). Preparation and characterization of nano-sized Co(II), Cu(II), Mn(II) and Ni(II) coordination PAA/alginate biopolymers and study of their biological and anticancer performance. *Crystals, 13*.

Amante, C., Andretto, V., Rosso, A., Augusti, G., Marzocco, S., Lollo, G., & Del Gaudio, P (2022). Alginate-pectin microparticles loaded with nanoemulsions as nanocomposites for wound healing. *Drug Delivery and Translational Research*, 1–15.

Amaral, D. L. A. S., Zanette, R. S. S., Almeida, C. G., Almeida, L. B. F., Oliveira, L. F. C.d., Marcomini, R. F., Nogueira, V. B., Santos, M. O., Brandão, H. M., Maranduba, C. MC., & Munk, M (2019). In vitro evaluation of barium titanate nanoparticle/alginate 3D scaffold for osteogenic human stem cell differentiation. *Biomedical Materials, 14*(3), Article 035011.

Axpe, E., & Oyen, M. L. (2016). Applications of Alginate-Based Bioinks in 3D Bioprinting. *International Journal of Molecular Sciences, 17*.

Bednarzig, V., Schrüfer, S., Schneider, T. C., Schubert, D. W., Detsch, R., & Boccaccini, A. R. (2022). Improved 3D printing and cell biology characterization of inorganic-filler containing alginate-based composites for bone regeneration: Particle shape and effective surface area are the dominant factors for printing performance. *International Journal of Molecular Sciences, 23*.

Boontheekul, T., Kong, H.-J., & Mooney, D. J. (2005). Controlling alginate gel degradation utilizing partial oxidation and bimodal molecular weight distribution. *Biomaterials, 26*(15), 2455–2465.

Braccini, I., & Pérez, S. (2001). Molecular basis of Ca^{2+}-induced gelation in alginates and pectins: The Egg-Box model revisited. *Biomacromolecules, 2*(4), 1089–1096.

Cai, F.-F., Heid, S., & Boccaccini, A. R. (2021). Potential of Laponite® incorporated oxidized alginate–gelatin (ADA-GEL) composite hydrogels for extrusion-based 3D printing. *Journal of Biomedical Materials Research Part B: Applied Biomaterials, 109*(8), 1090–1104.

Cao, L., Lu, W., Mata, A., Nishinari, K., & Fang, Y. (2020). Egg-box model-based gelation of alginate and pectin: A review. *Carbohydrate Polymers, 242*, Article 116389.

Cerciello, A., Del Gaudio, P., Granata, V., Sala, M., Aquino, R. P., & Russo, P. (2017). Synergistic effect of divalent cations in improving technological properties of cross-linked alginate beads. *International Journal of Biological Macromolecules, 101*, 100–106.

Chan, L. W., Ching, A. L., Liew, C. V., & Heng, P. W. S. (2007). Mechanistic study on hydration and drug release behavior of sodium alginate compacts. *Drug Development and Industrial Pharmacy, 33*(6), 667–676.

Cohen, D. L., Lo, W., Tsavaris, A., Peng, D., Lipson, H., & Bonassar, L. J. (2010). Increased mixing improves hydrogel homogeneity and quality of three-dimensional printed constructs. *Tissue Engineering Part C: Methods, 17*(2), 239–248.

Daemi, H., & Barikani, M. (2012). Synthesis and characterization of calcium alginate nanoparticles, sodium homopolymannuronate salt and its calcium nanoparticles. *Scientia Iranica, 19*(6), 2023–2028.

Dash, S., Gutti, P., Behera, B., & Mishra, D. (2024). Anionic species from multivalent metal salts are differentially retained during aqueous ionic gelation of sodium alginate and could fine-tune the hydrogel properties. *International Journal of Biological Macromolecules, 265*, Article 130767.

Donati, I., & Christensen, B. E. (2023). Alginate-metal cation interactions: Macromolecular approach. *Carbohydrate Polymers, 321*, Article 121280.

Falcone, G., Kuth, S., Boccaccini, A. R., Aquino, R. P., Esposito, T., & Russo, P. (2023). Application of calcium alginate hydrogels in semisolid extrusion 3D printed for the production of easy-to-swallow tablets. *Advanced Engineering Materials, 25*(9), Article 2201476.

Falcone, G., Mazzei, P., Piccolo, A., Esposito, T., Mencherini, T., Aquino, R. P., Del Gaudio, P., & Russo, P. (2022). Advanced printable hydrogels from pre-crosslinked alginate as a new tool in semi solid extrusion 3D printing process. *Carbohydrate Polymers, 276*, Article 118746.

Fang, Y., Al-Assaf, S., Phillips, G. O., Nishinari, K., Funami, T., Williams, P. A., & Li, L. (2007). Multiple steps and critical behaviors of the binding of calcium to alginate. *The Journal of Physical Chemistry B, 111*(10), 2456–2462.

Farshidfar, N., Iravani, S., & Varma, R. S. (2023). Alginate-based biomaterials in tissue engineering and regenerative medicine. *Marine Drugs, 21*.

Fuks, L., Filipiuk, D., & Majdan, M. (2006). Transition metal complexes with alginate biosorbent. *Journal of Molecular Structure, 792*, 104–109.

Gao, T., Gillispie, G. J., Copus, J. S., Pr, A. K., Seol, Y.-J., Atala, A., Yoo, J. J., & Lee, S. J. (2018). Optimization of gelatin–alginate composite bioink printability using rheological parameters: a systematic approach. *Biofabrication, 10*(3), Article 034106.

Gillispie, G. J., Copus, J., Uzun-Per, M., Yoo, J. J., Atala, A., Niazi, M. K. K., & Lee, S. J. (2023). The correlation between rheological properties and extrusion-based printability in bioink artifact quantification. *Materials & Design, 233*, Article 112237.

Giuseppe, M. D., Law, N., Webb, B. A., Macrae, R., Liew, L. J., Sercombe, T. B., … Doyle, B. J. (2018). Mechanical behaviour of alginate-gelatin hydrogels for 3D bioprinting. *Journal of the Mechanical Behavior of Biomedical Materials, 79*, 150–157.

Gómez-Blanco, J. C., Pagador, J. B., Galván-Chacón, V. P., Sánchez-Peralta, L. F., Matamoros, M., Marcos, A., & Sánchez-Margallo, F. M. (2023). Computational simulation-based comparative analysis of standard 3D printing and conical nozzles for pneumatic and piston-driven bioprinting. *IJB, 9*(4).

Gutierrez, E., Burdiles, P. A., Quero, F., Palma, P., Olate-Moya, F., & Palza, H. (2019). 3D printing of antimicrobial alginate/bacterial-cellulose composite hydrogels by incorporating copper nanostructures. *ACS Biomaterials Science & Engineering, 5*(11), 6290–6299.

Hafezi, F., Scoutaris, N., Douroumis, D., & Boateng, J. (2019). 3D printed chitosan dressing crosslinked with genipin for potential healing of chronic wounds. *International Journal of Pharmaceutics, 560*, 406–415.

Hazur, J., Detsch, R., Karakaya, E., Kaschta, J., Teßmar, J., Schneidereit, D., Friedrich, O., Schubert, D. W., & Boccaccini, A. R. (2020). Improving alginate printability for biofabrication: establishment of a universal and homogeneous pre-crosslinking technique. *Biofabrication, 12*(4), Article 045004.

Hazur, J., Röder, J., Czwalinna, J., Schubert, D. W., & Boccaccini, A. R. (2023). Pre-crosslinking with hydrogel microparticles enhances the printability of alginate-based inks. *Macromolecular Materials and Engineering*, Article 2200675. n/a(n/a).

Hernández-Escobar, D., Champagne, S., Yilmazer, H., Dikici, B., Boehlert, C. J., & Hermawan, H. (2019). Current status and perspectives of zinc-based absorbable alloys for biomedical applications. *Acta Biomaterialia, 97*, 1–22.

Herrada-Manchón, H., Fernández, M. A., & Aguilar, E. (2023). Essential guide to hydrogel rheology in extrusion 3D printing: How to measure it and why it matters? *Gels, 9*.

Hu, C., Hahn, L., Yang, M., Altmann, A., Stahlhut, P., Groll, J., & Luxenhofer, R. (2021). Improving printability of a thermoresponsive hydrogel biomaterial ink by nanoclay addition. *Journal of Materials Science, 56*(1), 691–705.

Hu, C., Lu, W., Mata, A., Nishinari, K., & Fang, Y. (2021). Ions-induced gelation of alginate: Mechanisms and applications. *International Journal of Biological Macromolecules, 177*, 578–588.

Jackson, S., & Dickens, T. (2021). Rheological and structural characterization of 3D-printable polymer electrolyte inks. *Polymer Testing, 104*, Article 107377.

Jain, D., & Bar-Shalom, D. (2014). Alginate drug delivery systems: application in context of pharmaceutical and biomedical research. *Drug Development and Industrial Pharmacy, 40*(12), 1576–1584.

Karakaya, E., Schöbel, L., Zhong, Y., Hazur, J., Heid, S., Forster, L., Teßmar, J., Boccaccini, A. R., & Detsch, R. (2023). How to determine a suitable alginate for biofabrication approaches using an extensive alginate library? *Biomacromolecules, 24*(7), 2982–2997.

Kiyotake, E. A., Douglas, A. W., Thomas, E. E., Nimmo, S. L., & Detamore, M. S. (2019). Development and quantitative characterization of the precursor rheology of hyaluronic acid hydrogels for bioprinting. *Acta Biomaterialia, 95*, 176–187.

Leal, D., Matsuhiro, B., Rossi, M., & Caruso, F. (2008). FT-IR spectra of alginic acid block fractions in three species of brown seaweeds. *Carbohydrate Research, 343*(2), 308–316.

Leppiniemi, J., Lahtinen, P., Paajanen, A., Mahlberg, R., Metsä-Kortelainen, S., Pinomaa, T., Pajari, H., Vikholm-Lundin, I., Pursula, P., & Hytönen, V. P. (2017). 3D-printable bioactivated nanocellulose–alginate hydrogels. *ACS Applied Materials & Interfaces, 9*(26), 21959–21970.

Li, H., Tan, Y. J., Liu, S., & Li, L. (2018). Three-dimensional bioprinting of oppositely charged hydrogels with super strong interface bonding. *ACS Applied Materials & Interfaces, 10*(13), 11164–11174.

Mallakpour, S., Azadi, E., & Hussain, C. M. (2021). State-of-the-art of 3D printing technology of alginate-based hydrogels—An emerging technique for industrial applications. *Advances in Colloid and Interface Science, 293*, Article 102436.

Martsouka, F., Papagiannopoulos, K., Hatziantoniou, S., Barlog, M., Lagiopoulos, G., Tatoulis, T., Tekerlekopoulou, A. G., Lampropoulou, P., & Papoulis, D. (2021). The antimicrobial properties of modified pharmaceutical bentonite with zinc and copper. *Pharmaceutics, 13*.

Matas, A., Molina-Montero, M. D., Igual, M., García-Segovia, P., & Martínez-Monzó, J. (2022). Printability prediction of three gels for 3D food printing. *Biology and Life Sciences Forum, 18*.

Mezger, T. (2020). *The rheology handbook: for users of rotational and oscillatory rheometers*. European Coatings.

Mørch, Ý. A., Donati, I., Strand, B. L., & Skjåk-Bræk, G. (2007). Molecular engineering as an approach to design new functional properties of alginate. *Biomacromolecules, 8*(9), 2809–2814.

Müller, M., Fisch, P., Molnar, M., Eggert, S., Binelli, M., Maniura-Weber, K., & Zenobi-Wong, M. (2020). Development and thorough characterization of the processing steps of an ink for 3D printing for bone tissue engineering. *Materials Science and Engineering: C, 108*, Article 110510.

Nakamoto, K. (1978). *In infrared and Raman spectra of inorganic and coordination compounds* (3rd ed., p. 233). New York, USA: Wiley Interscience.

Ouyang, L., Yao, R., Zhao, Y., & Sun, W. (2016). Effect of bioink properties on printability and cell viability for 3D bioplotting of embryonic stem cells. *Biofabrication, 8*(3), Article 035020.

Papageorgiou, S. K., Kouvelos, E. P., Favvas, E. P., Sapalidis, A. A., Romanos, G. E., & Katsaros, F. K. (2010). Metal–carboxylate interactions in metal–alginate complexes studied with FTIR spectroscopy. *Carbohydrate Research, 345*(4), 469–473.

Paxton, N., Smolan, W., Böck, T., Melchels, F., Groll, J., & Jungst, T. (2017). Proposal to assess printability of bioinks for extrusion-based bioprinting and evaluation of rheological properties governing bioprintability. *Biofabrication, 9*(4), Article 044107.

Ramya, M., Sarwat, S. G., Udhayabanu, V., Subramanian, S., Raj, B., & Ravi, K. R. (2015). Role of partially amorphous structure and alloying elements on the corrosion behavior of Mg–Zn–Ca bulk metallic glass for biomedical applications. *Materials & Design, 86*, 829–835.

Reig-Vano, B., Huck-Iriart, C., de la Flor, S., Trojanowska, A., Tylkowski, B., & Giamberini, M. (2023). Structural and mechanical analysis on mannuronate-rich alginate gels and xerogels beads based on Calcium, Copper and Zinc as crosslinkers. *International Journal of Biological Macromolecules, 246*, Article 125659.

Sartori, C., Finch, D. S., Ralph, B., & Gilding, K. (1997). Determination of the cation content of alginate thin films by FTi.r. spectroscopy. *Polymer, 38*(1), 43–51.

Schrüfer, S., Sonnleitner, D., Lang, G., & Schubert, D. W. (2020). A novel simple approach to material parameters from commonly accessible rheometer data. *Polymers, 12*.

Schubert, D. W. (2022). Simple model for the spreading of inks in bioprinting-revealing relevant scaling laws—Part I theory. *Macromolecular Theory and Simulations, 31*(1), Article 2100032.

Schwab, A., Levato, R., D'Este, M., Piluso, S., Eglin, D., & Malda, J. (2020). Printability and shape fidelity of bioinks in 3D bioprinting. *Chemical Reviews, 120*(19), 11028–11055.

Smith, P. T., Basu, A., Saha, A., & Nelson, A. (2018). Chemical modification and printability of shear-thinning hydrogel inks for direct-write 3D printing. *Polymer, 152*, 42–50.

Socrates, G. (2004). *Infrared and Raman characteristic group frequencies: tables and charts*. John Wiley & Sons.

Sonego, J. M., Santagapita, P. R., Perullini, M., & Jobbágy, M. (2016). Ca (II) and Ce (III) homogeneous alginate hydrogels from the parent alginic acid precursor: a structural study. *Dalton Transactions, 45*(24), 10050–10057.

Sonnleitner, D., Schrüfer, S., Berglund, L., Schubert, D. W., & Lang, G. (2021). Correlating rheology and printing performance of fiber-reinforced bioinks to assess predictive modelling for biofabrication. *Journal of Materials Research, 36*(19), 3821–3832.

Srivastava, R., & McShane, M. J. (2005). Application of self-assembled ultra-thin film coatings to stabilize macromolecule encapsulation in alginate microspheres. *Journal of Microencapsulation, 22*(4), 397–411.

Stojkov, G., Niyazov, Z., Picchioni, F., & Bose, R. K. (2021). Relationship between structure and rheology of hydrogels for various applications. *Gels, 7*.

Tabriz, A. G., Hermida, M. A., Leslie, N. R., & Shu, W. (2015). Three-dimensional bioprinting of complex cell laden alginate hydrogel structures. *Biofabrication, 7*(4), Article 045012.

Tan, J., Luo, Y., Guo, Y., Zhou, Y., Liao, X., Li, D., … Liu, Y. (2023). Development of alginate-based hydrogels: Crosslinking strategies and biomedical applications. *International Journal of Biological Macromolecules, 239*, Article 124275.

Tuladhar, S., Nelson, C., & Habib, M. A. (2022). Pre. *-crosslinked hybrid hydrogels for 3D bio-printing process: Rheological analysis*.

Townsend, J. M., Beck, E. C., Gehrke, S. H., Berkland, C. J., & Detamore, M. S. (2019). Flow behavior prior to crosslinking: The need for precursor rheology for placement of hydrogels in medical applications and for 3D bioprinting. *Progress in Polymer Science, 91*, 126–140.

Unalan, I., Schruefer, S., Schubert, D. W., & Boccaccini, A. R. (2023). 3D-printed multifunctional hydrogels with phytotherapeutic properties: development of essential oil-incorporated ALG-XAN hydrogels for wound healing applications. *ACS Biomaterials Science & Engineering, 9*(7), 4149–4167.

Vigo, D., Torre, M. L., Faustini, M., Munari, E., Russo, V., Norberti, R., Villani, S., Asti, A., Bini, P. P., & Conte, U. (2004). Barium alginate capsules for 3D immobilisation of living cells: morphology, membrane properties and permeability. *Journal of Drug Delivery Science and Technology, 14*(3), 167–172.

Wang, J., Liu, Y., Zhang, X., Rahman, S. E., Su, S., Wei, J., … Qiu, J. (2021). 3D printed agar/calcium alginate hydrogels with high shape fidelity and tailorable mechanical properties. *Polymer, 214*, Article 123238.

Wang, L., Xu, M.-e., Luo, L., Zhou, Y., & Si, P. (2018). Iterative feedback bio-printing-derived cell-laden hydrogel scaffolds with optimal geometrical fidelity and cellular controllability. *Scientific Reports, 8*(1), 2802.

Wei, Q., Zhou, J., An, Y., Li, M., Zhang, J., & Yang, S. (2023). Modification, 3D printing process and application of sodium alginate based hydrogels in soft tissue engineering: A review. *International Journal of Biological Macromolecules, 232*, Article 123450.

Yang, X., Lu, Z., Wu, H., Li, W., Zheng, L., & Zhao, J. (2018). Collagen-alginate as bioink for three-dimensional (3D) cell printing based cartilage tissue engineering. *Materials Science and Engineering: C, 83*, 195–201.

Zhang, J. Y., Pandya, J. K., McClements, D. J., Lu, J., & Kinchla, A. J. (2022). Advancements in 3D food printing: a comprehensive overview of properties and opportunities. *Critical Reviews in Food Science and Nutrition, 62*(17), 4752–4768.